Fourier transform infrared investigation of dielectric and lattice dynamical properties of $CuAlO_2$ delafossite under high pressure

C. Ferrer-Roca,[1,2] J. Pellicer-Porres,[1,2] A. Segura,[1,2] V. Panchal,[3] D. Kim,[4] P. Rodríguez-Hernández,[1,5] A. Muñoz,[1,5] and A. Polian[6]

[1]*MALTA-Consolider Team*

[2]*ICMUV, University of Valencia, 46100 Valencia, Spain*

[3]*Royal College of Arts, Science and Commerce, 401107 Mumbai, India*

[4]*Department of Chemistry, Pukyong National University, 48513 Busan, Korea*

[5]*Departamento de Física Fundamental II, Universidad de la Laguna, 38200 La Laguna (Tenerife), Spain*

[6]*IMPMC, CNRS Sorbonne Université, 75005 Paris, France*

(Received 11 March 2024; revised 10 July 2024; accepted 13 August 2024; published 27 September 2024)

This paper reports an investigation of the pressure dependence of lattice-dynamical and dielectric properties of $CuAlO_2$ delafossite by means of Fourier transform infrared spectroscopy and *ab initio* calculations. The availability of single-crystal and powdered samples allowed for an almost complete characterization of the pressure behavior of polar phonons and dielectric function from the far-infrared to the near-ultraviolet spectral range. The pressure-induced increase of the electronic contribution to the dielectric constant for polarization perpendicular to the c axis is fully accounted for by volume reduction, showing that the electronic polarizability remains virtually constant under pressure. The behavior of the polar phonon contribution to the static dielectric constant is more complex. The contribution of the high-frequency $E^h_{u,\mathrm{TO}}$ mode (489 cm^{-1}), with positive pressure coefficient, slightly decreases under pressure. On the opposite, the contribution of the low-frequency $E^l_{u,\mathrm{TO}}$ mode (143 cm^{-1} at ambient pressure) largely increases as it becomes softer under pressure, leading to an overall increase of the static dielectric constant. For polarization parallel to the c axis, the electronic contribution is insensitive to pressure. The polar mode $A^h_{2u,\mathrm{TO}}$ (700 cm^{-1}) has positive pressure coefficient. Then, an overall decrease of the static dielectric constant for polarization parallel to the c axis is expected.

DOI: 10.1103/PhysRevB.110.104312

I. INTRODUCTION

Delafossite structure compounds $CuM_{\mathrm{III}}O_2$ (M_{III} = Al, Ga, In, Sc, Cr, Fe, etc.) have been intensively studied since the late 1990s, when they were identified as one of the first families of performant p-type transparent conductive oxides (p-TCOs) [1–4]. Even if, strictly speaking, they cannot be considered as wide-gap materials [5,6], many delafossite thin films are transparent in the near-infrared–visible–near-UV range and have been used in transparent electronic devices, especially in p-n heterojunctions with n-ZnO [7–9], UV light-emitting devices [10,11], and also in photoelectrochemical [12] or photovoltaic [12,13] devices.

More recently, the interest in these materials has been refueled by the multiferroic behavior of transition-metal delafossites, like $CuCrO_2$. While still presenting improved p-TCO features [14], in these materials antiferromagnetic order triggers ferroelectric [15] and ferroelastic [16] transitions, giving rise to anisotropic magnon dispersion [17] and complex magnon-phonon [18] or magnon-exciton [19] elementary excitations. This complex multiferroic behavior has been shown to allow for fine-tuning of electric polarization reversal by electric or magnetic fields [20]. It has also been shown that under high pressure they also exhibit a very complex multiferroic phenomenology [21].

The structural and lattice dynamical properties of delafossites under high pressure have been widely investigated, as reviewed in Ref. [22], by means of x-ray diffraction (XRD), x-ray absorption (XAS), and Raman-effect experiments. Delafossite vibration modes of the rhombohedral polytype at the Γ point (point group $R\bar{3}m$) can be decomposed as $\Gamma = A_{1g} + E_g + 3A_{2u} + 3E_u$. Figure 1 shows the vibration schemes of these zone center modes. Given the centrosymmetric character of the space group, Raman scattering only yields information on the pressure behavior of A_{1g} and E_g even modes [23,24].

In contrast to the wealth of results on Raman experiments found in the literature, infrared (IR)-active modes of delafossite compounds have not yet been investigated. In this paper we present an investigation on $CuAlO_2$ by means of Fourier transform infrared (FTIR) reflectance and transmittance measurements under high pressure. The quality of experimental reflectance and transmittance spectra at different pressures allows for fits of theoretical models yielding the wave number of the σ_{TO} and σ_{LO} IR-active modes and their pressure dependence. Fits also yield a good estimation of the static- and electronic dielectric constants. On the other hand, in some configurations, the mirrorlike sample interfaces create a well-defined Fabry-Perot cavity. In these cases, interference fringe patterns are observed both in the low- and high-frequency sample transparency range. This allows for

	σ	$\partial\sigma / \partial P$
E_u^l TO	143±2 (exp) 144±2 (calc*) 152±8 (calc)	-0.7±0.1 (exp) -0.8±0.1 (calc*) -0.6±0.1 (calc)
E_u^l LO	150±5 (exp) 149±2 (calc*) 155±8 (calc)	-0.35±0.05 (exp) -0.4±0.1 (calc*) -0.2±0.1 (calc)
E_g	418±0.2 (exp*) 433±4 (calc*) 420±20 (calc)	2.72±0.07 (exp*) 2.7±0.1 (calc*) 2.5±0.2 (exp)
A_{2u}^l TO	Not observed 474±5 (calc*) 460±20 (calc)	Not observed 3.2±0.1 (calc*) 3.1±0.1 (calc)
A_{2u}^l LO	Not observed 474±5 (calc*) 460±20 (calc)	Not observed 3.3±0.1 (calc*) 3.1±0.1 (calc)

	σ	$\partial\sigma / \partial P$
E_u^h TO	489±3 (exp) 532±5 (calc*) 500±20 (calc)	4.6±0.1 (exp) 5.1±0.2 (calc*) 4.8±0.3 (calc)
E_u^h LO	663±4 (exp) 645±6 (calc*) 640±30 (calc)	3.4±0.1 (exp) 4.7±0.1 (calc*) 4.6±0.9 (calc)
A_{2u}^h TO	705±15 (exp) 737±7 (calc*) 690±30 (calc)	4.8±0.1(exp) 5.0±0.2 (calc*) 5.0±0.3 (calc)
A_{2u}^h LO	870±2 (exp) 874±9 (calc*) 850±40 (calc)	5.0±0.3 (exp) 5.2±0.2 (calc*) 4.2±0.9 (calc)
A_{1g}	767.2±0.3 (exp) 770±8 (calc) 750±40 (calc)	4.96±0.12 (exp) 4.8±0.1 (calc*) 4.6±0.5 (calc)

*Ref 24.

FIG. 1. Delafossite $CuAlO_2$ normal modes. White, light-gray, and dark-gray spheres correspond to O, Cu, and Al atoms, respectively. Wave numbers σ are given in cm^{-1} and pressure coefficients in cm^{-1}/GPa.

a precise determination of the frequency-dependent optical path and, consequently, of the refractive index and dielectric function dispersion. This technique provides an independent determination of the static- and electronic dielectric constants, yielding a supplementary self-consistence test for the set of physical quantities investigated here.

The experimental setups and calculation methods are described in Sec. II. Experimental results are presented, interpreted, and discussed in Sec. III, which is divided into subsections, each one devoted to results of different physical parameters and their pressure dependence. We first present and discuss, in Sec. III A, the results at ambient pressure, as they involve all physical quantities whose pressure dependence is the object of this paper (TO/LO polar phonons and static dielectric constants). Then, in Sec. III B, we discuss the pressure dependence of the refractive index, from which the pressure dependence of the electronic contribution to the dielectric constant is obtained. It is worth stressing that this technique (based on interference fringe patterns) provides us with an independent parameter to check the consistency of the different methods. In Sec. III C, we discuss the pressure dependence of the static dielectric function. The fact that its decrease under pressure in the far-infrared (FIR) range seems to be inconsistent with the Lyddane-Sachs-Teller relationship reveals the role of the low-frequency E_u^l mode. In this subsection we show that the E_u^l mode softening under high pressure is the key to give a consistent account of the pressure dependence of the dielectric function. The pressure dependence of the high-frequency E_u^h modes is then presented and discussed in Sec. III D. The pressure evolution of single-crystal transmission spectra (that exhibit a series of absorption peaks above the TO-LO opacity range) is the basis to study the pressure dependence of both the A_{2u}^h polar phonons and two-phonon absorption processes (Sec. III E). In order to keep the length of the paper reasonable, results of pellets are reported and discussed in the Supplemental Material [25].

II. EXPERIMENTAL AND CALCULATION DETAILS

$CuAlO_2$ single crystals were grown from $CuAl_2O_4$-CuO melt by a slow cooling method from 1423 K in air, following the procedure described in Ref. [26]. This method yields single crystals with different sizes. Platelets with typical dimensions of $200 \times 200 \times (10-30)\,\mu m^3$, whose largest surface is oriented perpendicular to the hexagonal c axis, were chosen for high pressure experiments. Thicker single crystals exhibiting larger faces nearly parallel to the c-axis were selected for FTIR experiments at ambient pressure.

Polycrystalline $CuAlO_2$ was prepared by the ceramic method. Stoichiometric amounts of Al_2O_3 and Cu_2O (99.995 and 99.9% pure, respectively) were milled and homogenized during 2 h in a planetary mill using hexane as medium. The mixture was calcined in a tubular furnace, under Ar-controlled atmosphere, at 1100 °C for 12 h using high-purity alumina crucibles.

Most of the experiments under high pressure were performed at the Spectroscopy and Microscopy in Infrared using Synchrotron (SMIS) beamline [27] in the French National Synchrotron Facility (SOLEIL). High pressure was generated with a membrane diamond-anvil cell (MDAC) [28]. The anvils consisted of IIac diamonds with 500-μm culet diameter. The pressure chamber in the MDAC was defined by a hole drilled in a previously indented Inconel steel gasket. The powdered samples were mixed with a solid pressure-transmitting medium (KBr or CsI), filling the pressure chamber with the mixture. The proportion of delafossite powder can be changed

in order to obtain thinner or thicker samples in terms of the effective light absorption length. KBr was used for the 600–6000-cm^{-1} midinfrared (MIR) range and CsI was used for the 100–600-cm^{-1} far-infrared (FIR) range. For crystalline samples either KBr or neon were used as pressure-transmitting medium. Pressure was systematically measured before and after the acquisition of each spectrum using the fluorescence emission of a ruby chip [29,30].

The SMIS optical setup used a NicPlan IR microscope coupled to an FTIR spectrometer (Thermo Nicolet Magma 560). The microscope was operated in confocal mode, using a 32× infinity-corrected Schwartzschild objective (numerical aperture 0.65) and a matching tenfold condenser. Two different IR detectors were used. A Cu-Ge bolometer (Infrared Laboratories) cooled to liquid He temperature was used in the FIR range, which allowed for an effective spectral range between 100 and 600 cm^{-1}. A mercury-cadmium telluride (MCT) detector was used for the MIR range, with spectral range from 600 to 6000 cm^{-1}. Typically, the spectral resolution was set to 1 cm^{-1} and up to 256 scans per spectrum were accumulated and averaged. Given the high brilliance of the synchrotron radiation, the beam size can be set down to $15 \times 15\,\mu m^2$ at the focal point, allowing the study of far smaller samples than those used in a laboratory setup with an IR Globar source. In transmittance experiments, thanks to the small but bright synchrotron infrared beam, the reference beam was measured at each pressure through the diamonds in the void space next to the sample. In reflectance experiments, we took the reference spectrum using the metallic surface of the gasket as a mirror.

In a second set of experiments on monocrystalline samples we used a home-built FTIR setup, described in Ref. [31], operating in the mid-IR region (400–6000 cm^{-1}). The setup consisted of (i) a commercially available FTIR module spectrometer (TEO 400 FTIR Module by Interspectrum), including a Globar IR source and a Michelson interferometer, and (ii) an all-reflecting optical bench, including a DAC stage and a MCT IR detector.

Total energy simulations without thermal contributions were performed with first-principle calculations carried out within the framework of density-functional theory [32], using the Vienna *Ab initio* Simulation Package [33], VASP. In our study we used the projector augmented-waves pseudopotential [34,35]. A plane-wave energy cutoff of 550 eV was used to ensure highly converged results. The k-special point sampling of the Brillouin zone (BZ) was performed using a $6 \times 6 \times 6$ dense grid to obtain highly converged results. The exchange-correlation energy was described using the generalized gradient approximation, with the Perdew-Burke-Ernzerhof for solids (PBEsol) functional [36].

At selected volumes, the unit-cell parameters and the atomic positions were fully optimized to obtain the relaxed structures, imposing that the forces on the atoms were less than 0.003 eV/Å, and deviations of the stress tensors from a diagonal hydrostatic form were lower than 0.1 GPa.

Lattice-dynamic calculations of the phonon modes were carried out at the zone center (Γ point) of the BZ with the direct force-constant approach using the PHONOPY package [37]. These computations provided not only the frequency of the normal modes, but also their symmetry and polarization vectors. This allowed us to identify the irreducible representations and the character of the phonon modes at the Γ point. To calculate the LO/TO splitting we used a $2 \times 2 \times 2$ supercell to include the nonanalytical-term corrections [38], using density-functional perturbation theory [39] to obtain the dielectric tensor and the Born effective charge tensor.

III. RESULTS AND DISCUSSION

A. Polar phonons and dielectric function of $CuAlO_2$ at ambient conditions

In order to model the experimental reflectance spectra, including the interference pattern, we used the factorized form of the dielectric function proposed in Refs. [40–42],

$$\varepsilon_p(\sigma) = \varepsilon_{pe} \prod_{j=1}^{j=N} \frac{\sigma_{pj\mathrm{LO}}^2 - \sigma^2 - i\Gamma_{pj\mathrm{LO}}\sigma}{\sigma_{p\mathrm{TO}}^2 - \sigma^2 - i\Gamma_{pj\mathrm{TO}}\sigma}, \tag{1}$$

where σ stands for the wave number and N for the number of polar modes in the explored spectral range; p stands for the light polarization conditions ($\perp$, $\parallel$), perpendicular or parallel to the c axis; ε_{pe} is the electronic dielectric constant, $\sigma_{pj\mathrm{TO/LO}}$ are the TO and LO frequencies of the polar mode j, and $\Gamma_{pj\mathrm{TO/LO}}$ are their associated damping coefficients. Given the optical absorption selection rules for the $\bar{3}m$ point group, the phonon frequencies for polarization perpendicular (parallel) to the c axis correspond to the E_u (A_{2u}) IR-active phonons.

Figure 2(a) shows the reflectance spectrum of two $CuAlO_2$ platelets at ambient conditions, in the Reststrahlen spectral range associated with the E_u^h phonon, for polarization perpendicular to the c axis. Samples were held in air in ambient pressure studies. Each spectrum was taken in one of the IR spectral ranges described in Sec. II (red symbols in the FIR range and black symbols in the MIR range). The spectra exhibited interference fringe patterns on both sides of the high-reflectance interval between the TO/LO modes. From the real and imaginary parts of the dielectric function given by Eq. (1), for $p = \perp$, the refractive and extinction indexes were calculated and introduced in the theoretical expression of the reflectance, at normal incidence, of a dielectric slab between two different media developed by Heavens [43]. The value of the electronic dielectric constant for polarization perpendicular to the c axis was taken from Ref. [44]. The interference fringe pattern in the MIR range allowed for an accurate determination of the sample thickness by using the refractive index dispersion (also taken from Ref. [44]) (see Note [45]).

Table I includes all parameters used to calculate the reflectance [dashed lines in Fig. 2(a)]. The difference between the values of polar phonon frequencies and static dielectric constant obtained here and those reported in Ref. [44] simply reflected the fact that interference fringe measurements in Ref. [44] were limited to the midinfrared spectral range and only the product $\varepsilon_0\sigma_{\mathrm{TO}}^2$ could be determined. It should be stressed that in the present results, the interference fringe pattern in the FIR range conveys supplementary relevant information, providing further self-consistency to the physical parameters given in Table I. Please note that the amplitude of the oscillations depended on extrinsic factors such as the

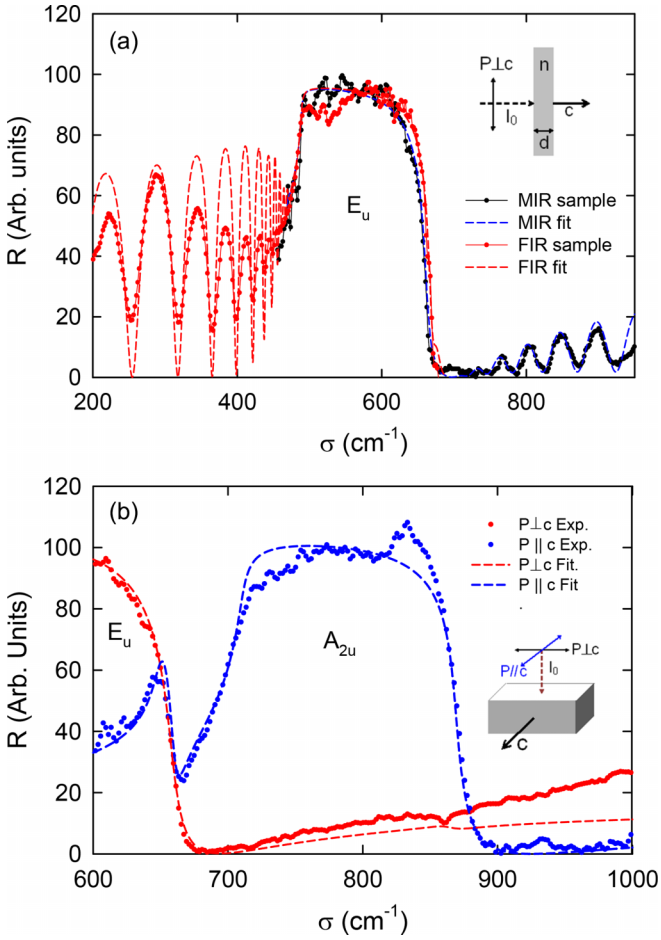

FIG. 2. Reflectance spectra at ambient conditions of different $CuAlO_2$ single-crystal samples in both FIR and MIR ranges: (a) two platelets with polarization perpendicular to the *c* axis and (b) a mirrorlike thick sample for both light polarizations parallel- (sample slightly tilted though) and perpendicular to *c* axis). The dashed lines represent a fit using a dielectric function oscillator, plus that of the interference pattern within the platelet [in (a)].

optical quality of the surface and was not relevant to the discussion of optical parameters.

Figure 2(b) shows the polarized light reflectance spectra of a thick $CuAlO_2$ single crystal with a mirrorlike surface nearly parallel to the *c* axis. By rotating the polarizer it was possible to identify the direction for which the incident beam was polarized perpendicular to the c axis. When rotating the polarizer 90 °, the reflectance spectrum was dominated by the response of the A^h_{2u} phonon. However, it was not possible to completely eliminate the E_u contribution, indicating that the selected sample face is not strictly parallel to the *c* axis, but slightly tilted with respect to it. The normal incidence reflectance on the oblique face (at an angle θ to the c axis) can be calculated from the effective dielectric function [46]:

$$\frac{1}{\varepsilon_\theta(\sigma)} = \frac{\cos^2\theta}{\varepsilon_\perp(\sigma)} + \frac{\sin^2\theta}{\varepsilon_\parallel(\sigma)}. \tag{2}$$

Dashed lines in Fig. 2(b) have been calculated using Eqs. (1) and (2), with $\theta = 90\,^\circ$ for s polarization conditions and $\theta = 8\,^\circ$ and $\theta = 14\,^\circ$ for samples M3 and M4, respectively, with the parameters listed in Table I.

The pressure dependence of the polar phonons' frequencies will be determined in Sec. III D by fitting the calculated reflectance to the experimental reflectance spectra at different pressures. Obtaining reliable values of the phonon frequencies through this method requires limiting the number of free parameters, which can be done by determining the pressure dependence of some of them by a different technique. This is the case of the electronic contribution to the dielectric function, whose pressure dependence will be determined in Sec. III B from the pressure evolution of interference fringe patters in the NIR-VIS range. This involves an accurate determination of the electronic dielectric function at ambient pressure that is presented and discussed in Sec. SM-I of Supplemental Material [25] The dispersion of the dielectric function was determined from the interference fringe pattern of a thin sample and interpreted through the Phillips–van Vechten model [47,48] including the contributions of the Penn gap [49] as well as the contribution of a direct exciton. Results were shown to be consistent with *ab initio* calculations by Kumar and coworkers [50].

TABLE I. Dielectric constants, frequencies, and damping coefficients of selected polar normal modes in $CuAlO_2$.

	Sample in this work or reference	*d* (μm)	ε_0	ε_∞	σ_{TO} (cm^{-1})	σ_{LO} (cm^{-1})	Γ_{TO} (cm^{-1})	Γ_{LO} (cm^{-1})
	M1	17.7± 0.1	9.4 ± 0.1	5.1 ± 0.1	489 ± 2	666 ± 5	3.0 ± 0.5	8 ± 1
$P\perp c$	M2	29.1 ± 0.1	9.3 ± 0.1	5.1 ± 0.1	489 ± 2	661 ± 5	3.0 ± 0.5	10 ± 1
	M3		9.3 ± 0.1	5.1 ± 0.1	489 ± 2	661 ± 5	3.0 ± 0.5	11 ± 1
	M4		9.3 ± 0.1	5.1 ± 0.1	487 ± 2	659 ± 5	3.0 ± 0.5	11 ± 1
E^h_u	Ref. [43]	13.1 ± 0.1	7.7 ± 0.8	5.1 ± 0.1	550 ±25			
	Theor. Ref. [24]				532 ±5	645 ± 6		
	Ref. [43]			3.6 ± 0.1				
$P//c$								
	M3		5.5 ± 0.1	3.6 ± 0.1	700 ± 10	865 ± 10	20 ± 2	20 ± 2
	M4		5.6 ± 0.1	3.6 ± 0.1	700 ± 10	869 ± 10		
A^h_{2u}								
	Theor. Ref. [24]				737± 7	874 ± 9		

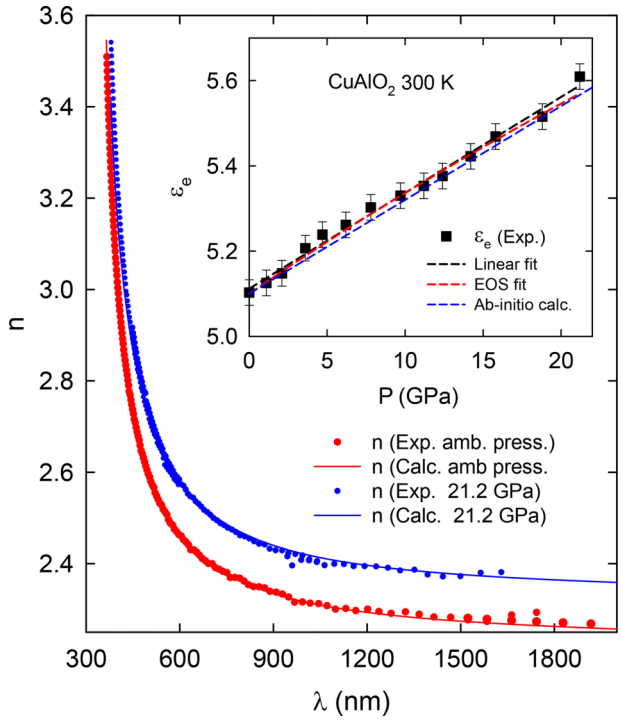

FIG. 3. $CuAlO_2$ refractive index for polarization perpendicular to the c axis at 0 and 21.2 GPa, including experimental points and also best fits obtained with a Penn gap and exciton contribution. Inset: pressure dependence of the electronic dielectric constant ε_e. The dotted lines represent a linear fit (black), an EOS calculated fit (red) assuming a pressure dependence only determined by volume decrease under pressure, and *ab initio* calculations (blue).

B. Pressure dependence of the electronic dielectric function

Figure 3 shows the refractive index for polarization perpendicular to the c axis at ambient pressure and at 21.2 GPa, as obtained from the interference fringe pattern at both pressures. As it can be seen in the figure, the refractive index increased with pressure in the whole explored spectral range, including the strong dispersion high-energy interval associated with the $CuAlO_2$ direct band gap (between 400 and 600 nm). The exciton peak responsible for the strong dispersion in the high-energy limit has been shown to shift to higher energies under high pressure [6], with a pressure coefficient of 2 meV/GPa. As a consequence, the exciton contribution to the refractive index should also have shifted to higher photon energies. If one assumed that the exciton peak width did not change under pressure, its blueshift would have resulted in a small negative contribution at a given wavelength. This did not appear to be the case, and indicated that in spite of the exciton blueshift, the exciton contribution increased under pressure. This was the expected behavior, given that as shown in Ref. [6], the indirect gap of $CuAlO_2$ had a pressure coefficient of 15 meV/GPa. Therefore, the energy difference between the direct and indirect gaps decreased from about 0.5 eV at ambient pressure to about 0.2 eV at 21.2 GPa, which indicated that the resonant character of the exciton decreased under pressure, and led to an increase in its absorption intensity.

In order to evaluate the behavior of the different contributions, we have calculated the dielectric function at different

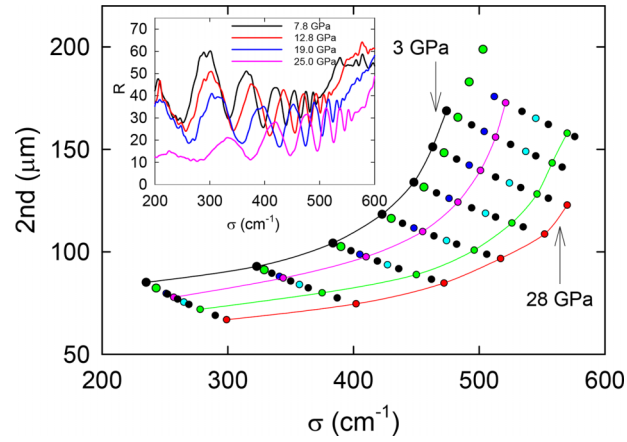

FIG. 4. The optical-path spectrum, unambiguously obtained from the interference fringe pattern in the reflectance spectra, decreases with pressure in the whole spectral range. Fringes are shown in the inset with an evident blueshift for different increasing pressures.

pressures using Eq. SM(2) [25]. The plasma frequencies at each pressure have been scaled to the dipole density given by the equation of state (EOS) of $CuAlO_2$ [51]. The exciton peak energy at each pressure was determined from the pressure coefficient of the direct gap [6]. The best fit was obtained by keeping the Penn gap unchanged and linearly decreasing the exciton width as the pressure increased. Table SM-I [25] shows the parameters used to calculate the dielectric function (refractive index) at 21.2 GPa through Eq. SM(2). The result is plotted as blue line in Fig. 3.

The inset of Fig. 3 shows the pressure dependence of the electronic contribution to the static dielectric constant. The dotted black line is a linear fit. The dotted red line corresponds to the calculated value on the assumption that the pressure dependence is determined only by the volume decrease under pressure. The fact that within the experimental errors, the red line reasonably fit the experimental results indicated that the pressure dependence of the electronic dielectric function was mainly determined by the positive contribution of the increased dipole density (arising from the volume decrease). It could be inferred that the overall electronic polarizability remained practically unchanged under high pressure. In terms of electronic transitions, the pressure behavior of the electronic polarizability was accounted for by the pressure behavior of the intense direct transitions that contributed to the imaginary part of the dielectric function. It seemed reasonable to assume that the slight decrease associated with the blueshift of the direct absorption around 3.5 eV was compensated by a slight redshift of the Penn gap.

C. Pressure dependence of the static dielectric constant: Effect of E_u low polar phonon

As previously discussed when commenting on the low-frequency interval of Fig. 2(a), pressure effects on the interference fringe pattern in the reflectance spectrum convey relevant information about the pressure behavior of the dielectric function. The inset of Fig. 4 shows that as pressure increases, the maxima and minima of the reflectance spectrum

shift to higher frequencies, indicating a pressure-induced decrease of the optical path. The interference order can be unambiguously determined, which allows for a precise determination of the optical-path spectrum at different pressures, as shown in Fig. 4. Two relevant pressure effects are observed. First, as pressure increases there is an overall decrease of the optical path in the whole spectral range. Second, the high dispersion interval associated with the E_u^h(TO) phonon shifts to higher frequencies, consistently with the positive pressure coefficient of this phonon mode, as shown in the inset.

Let us start the discussion with an estimation of the pressure-induced decrease of the optical path in the low-frequency range. At 300 cm^{-1}, the experimentally measured optical path decreases by 28% between ambient pressure and 28 GPa. Given the value of the material compressibility along the c axis (8.3×10^{-4} GPa^{-1}) [51], the sample thickness reduction would account only for a decrease of 2.3%. This would imply a decrease of the refractive index by more than 25% and then, a decrease in the dielectric constant by more than 50% between ambient pressure and 28 GPa. As shown in the previous section, the electronic dielectric constant increased under pressure. At ambient pressure the electronic contribution to the static dielectric constant makes up about 50% of its value (see Table I). Then, to give account of a decrease of the total static dielectric constant by 50% the contribution of the E_u^h polar phonon to it should decrease down to a vanishingly small value. Apart from being physically unlikely, this hypothesis is not consistent with the Lyddane-Sachs-Teller relationship.

These apparently inconsistent results may be explained by taking into account the behavior of the E_u^l phonon (149 cm^{-1} at ambient pressure). As shown below, this phonon softens and becomes more polar under pressure. We will show that this behavior accounts for most of the observed decrease of the optical path in the low-dispersion range (from 200 to 400 cm^{-1} in Fig. 4).

Owing to the use of different filters, the spectrum of the IR signal in the synchrotron beamline exhibits many absorption peaks in the frequency range around the E_u^l phonon. Slight instabilities of the electron beam during a set of measurements can change the intensity of those peaks in the sample-transmitted intensity (with respect to their intensity in the direct beam reference spectrum). As a consequence, the E_u^l signature, which is clearly observed in the sample-reflected intensity spectrum, can be distorted in the normalized reflectance. For this reason, Fig. 5 presents the spectrum reflected by the sample, without normalization. A transmission minimum, which clearly correlates to the reflectance structure, is also observed in the sample transmission spectrum (not shown). The contribution of the E_u^l phonon to the sample reflectance could be calculated through Eq. (1) using the E_u^l phonon parameters. In order to compare with the experimental one, the calculated spectrum is multiplied by a smoothed I_0 spectrum (a polynomial fit to the IR beam intensity not including the filter absorption peaks). As shown in Fig. 5, the reflectance structure associated with E_u^l shifts to lower energies and becomes more intense as pressure increases. As we have not been able to perform a proper normalization of the spectra in Fig. 5, the information obtained from simulating the reflectance is limited. We

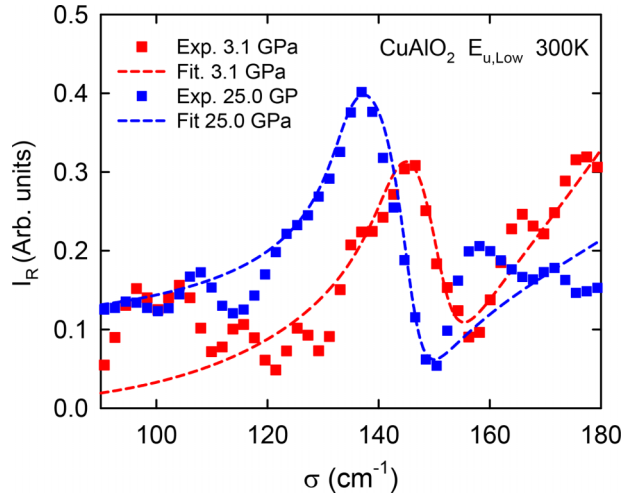

FIG. 5. Symbols: Intensity reflected by the sample without normalization so as to evidence an E_u^l phonon-mode feature around 150 cm^{-1} at two pressures: 3.1 GPa (red) and 25 GPa (blue). Dashed lines: calculated fit using a dielectric oscillator function. This E_u^l-related feature redshifts and increases its intensity with pressure.

propose a different, more fundamental approach, to extract information about the pressure behavior of the E_u^l mode. Figure 6 shows the pressure dependence of three features of the sample reflection and transmission experimental spectra (reflection minimum, reflection maximum, and transmission minimum), as well as the *ab initio* calculated pressure dependence of the E_u^l TO and LO phonons. The calculated E_u^l LO mode closely follows the behavior of the reflectance minimum, as expected. The slope of the calculated E_u^l TO mode corresponds to that of the transmittance minimum. We therefore attribute the pressure dependence of the transmittance

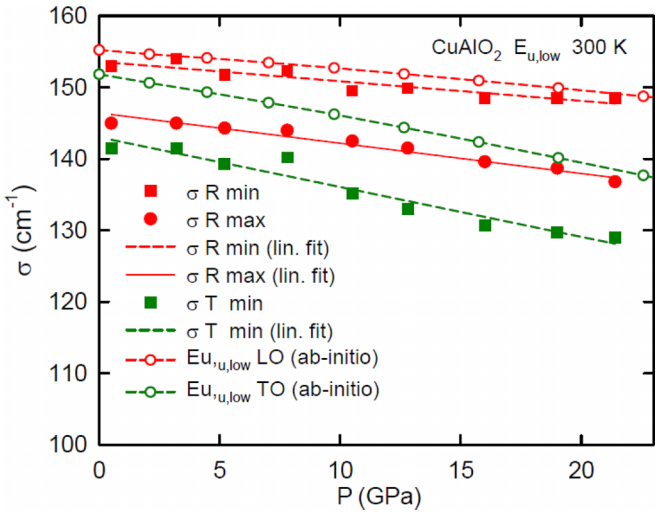

FIG. 6. Pressure dependence of three features of the sample reflectance and transmittance experimental spectra (reflection minimum, reflection maximum, and transmission minimum): experimental values, linear fits, and *ab initio* calculated pressure dependence of the E_u^l TO and LO phonons. Both phonons become softer under pressure with a larger coefficient for the TO frequency, indicating it becomes more polar under pressure.

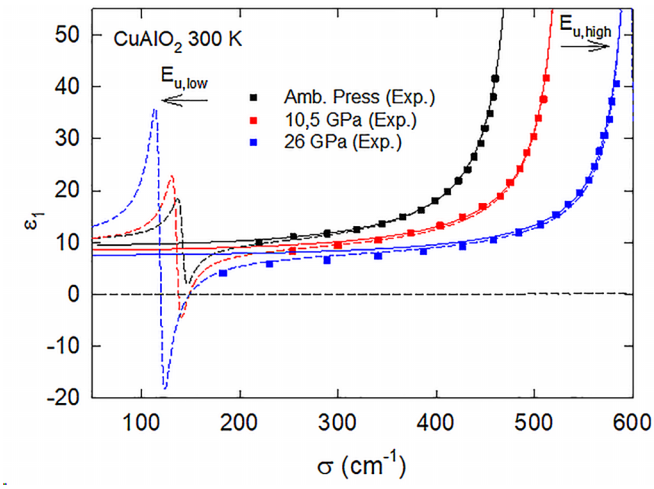

FIG. 7. The dielectric function of $CuAlO_2$ at three different pressures, including the effect of both E_u phonons, as calculated through Eq (1) (dashed lines; see text) in good agreement with experimental points (symbols) obtained from the interference fringe patterns. The figure also shows the calculated dielectric function when the contribution of E_u^l is not taken into account (continuous lines). The *ab initio* calculations are performed without thermal contribution.

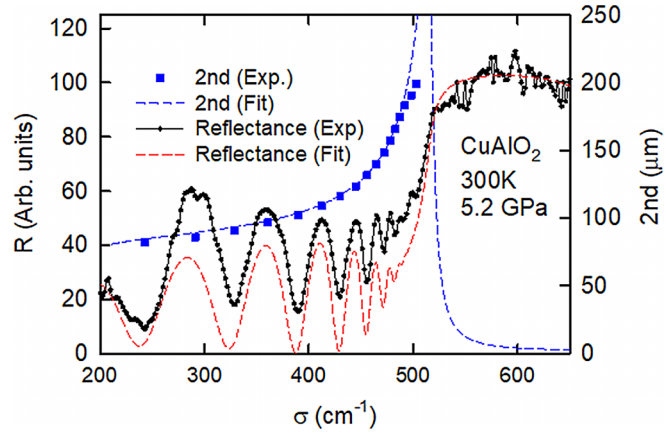

FIG. 8. Experimental reflectance spectrum of a sample at 5.2 GPa, measured at SMIS, using Ne as PTM. The oscillations in the range 200–500 cm^{-1} are an interference fringe pattern originated within the sample that allows for a precise determination of the optical path (second) at the reflectance maxima and minima. The fit to the reflectance (dashed red) is confirmed by the fit to the experimental optical path second (dashed blue).

minimum to the E_u^l TO mode. A summary of the wave numbers and pressure coefficients obtained is given in Fig. 1. From this analysis we conclude that both the TO and LO phonons become softer under pressure, but the TO frequency decreases with a larger absolute coefficient, clearly indicating that the phonon becomes more polar under pressure. The increase in polarity is crucial in describing the behavior of the dielectric functions, as explained below, and supports our analysis.

In order to get a quantitative account of the effects of the E_u^l phonon in the dielectric function, the corresponding term must be included in Eq. (1), with $N = 2$ ($j = 1$ corresponding to E_u^l, and $j = 2$, corresponding to E_u^h). Figure 7 shows the dielectric function of $CuAlO_2$ at three pressures, including the effect of both E_u phonons, as calculated through Eq. (1). The experimental points obtained from the interference fringe pattern (Fig. 4) are also shown in order to point out the good agreement. Figure 7 also shows the calculated dielectric function when the contribution of E_u^l is not considered (continuous lines). As expected, for lower wave numbers, it tends asymptotically to a constant value and does not fit the experimental values. This result shows that both the large decrease and dispersion of the dielectric function in the 200–400-interval can be quantitatively accounted for by taking into account the pressure behavior of the E_u^l phonon.

It should also be noticed that, as expected, for frequencies larger than about 80% of the E_u^h TO frequency the contribution of the E_u^l phonon to the dielectric function becomes irrelevant and it is not necessary to include it in the calculation.

D. Pressure dependence of the E_u high polar phonons: Reflection

The pressure dependence of the LO and TO modes of E_u^h phonon has been determined from fits to the reflectance spectra of several samples in different experiments, in both FTIR experimental setups (SMIS beamline and in-house) described in Sec. II.

Both setups have spectral range limitations owing to the IR detectors and IR filters used in each one. The FIR setup in the SMIS beamline is limited to the range between 100 and 700 cm^{-1} for the FIR range and 600 to 6000 cm^{-1} for the MIR range, while the in-house setup does not provide any reliable signal below 500 cm^{-1}.

Figure 8 shows an example of fit to the experimental spectrum of the sample at 5.2 GPa, measured at SMIS, using Ne as pressure-transmitting medium (PTM). Given the large refractive index of $CuAlO_2$ in this spectral range, the PTM-sample-PTM Fabry-Perot cavity determines the interference fringe pattern between 200 and 500 cm^{-1}, allowing for a precise determination of the optical path ($2nd$) at the reflectance maxima and minima. Both the fit to the reflectance (red dashed line in Fig. 8) and the fit to the experimental optical path (blue dashed lines in Fig. 8) were calculated with the same parameters, confirming the previously mentioned self-consistence of the fitting procedure.

Figure 9(a) shows an example of fitting to the experimental reflectance measured at SMIS in the MIR range. In this configuration, the interference fringe pattern above the LO frequency contains contributions of two Fabry-Perot cavities, the sample itself, and the sample–PTM–diamond cavity, with optical paths close to one another (resulting in a modulation of the interference amplitude). Consequently, the fringe pattern cannot be directly used to extract information on the sample dielectric function. Nevertheless, it seems interesting to stress that the fitting procedure can reproduce some features of the interference in the interval just below the LO frequency (through which the sample refractive index is very different from the one of the PTM).

Figure 9(b) shows an example of fitting to the experimental reflectance measured in the in-house setup. In this experiment, a gold film was deposited on the back face of the sample. In this way the reflected beam only contained contributions from

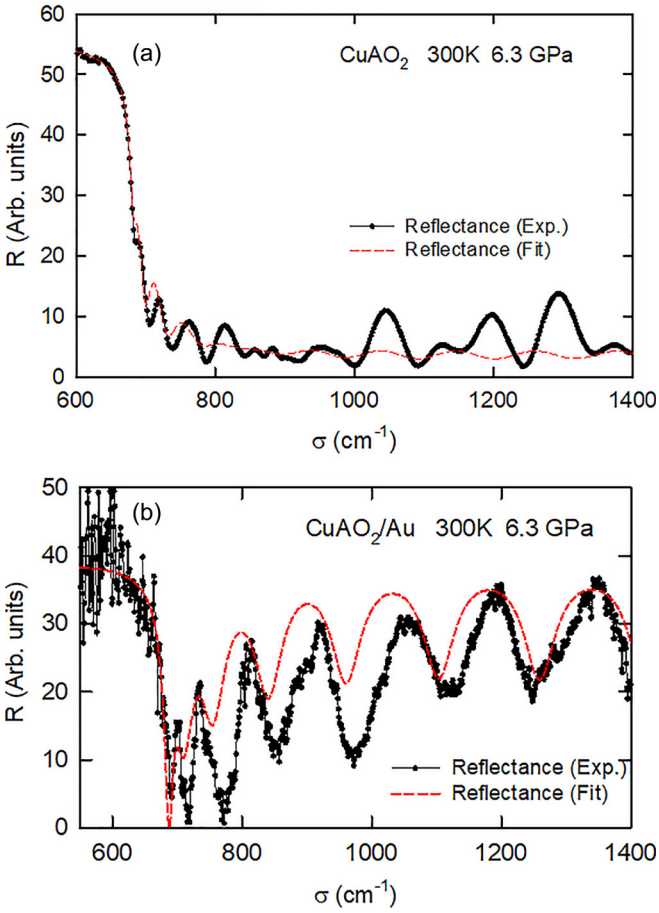

FIG. 9. Two fitting examples: (a) to the experimental reflectance measured at SMIS in the MIR range. The amplitude-modulated oscillations above the E_u^h TO frequency indicate that the interference fringe pattern is originated both in the sample cavity and the sample–PTM–diamond cavity, with similar optical paths, and (b) to the experimental reflectance measured in the in-house setup, with a sample with a gold-film deposition on the back face, to include only contributions from the sample cavity.

the diamond-sample and sample-gold interfaces. Then, the interference fringe pattern from the sample was not perturbed by the back Fabry-Perot cavity at the DAC pressure chamber (sample–PTM–diamond cavity), as shown in Ref. [52]. In this configuration the reflectance was also calculated through the theoretical expression developed by Heavens [43], including (for the back medium) the dielectric function of gold as modeled in Ref. [53].

$$\varepsilon_{\mathrm{Au}}(\sigma) = 1 - \frac{\sigma_{P,\mathrm{Au}}^2}{\sigma^2 + i\Gamma\sigma}, \tag{3}$$

where $\sigma_{P,\mathrm{Au}}$ was the effective plasma frequency of gold (68150 cm^{-1}) and Γ the electron relaxation frequency (3280 cm^{-1}). This model correctly accounted for the observed interference fringe pattern. It is relevant to notice that the position of the maxima and minima was modified by the phase shift induced by the sample-Au interface (with respect to their position in the reflectance spectrum of a sample without a gold back coating).

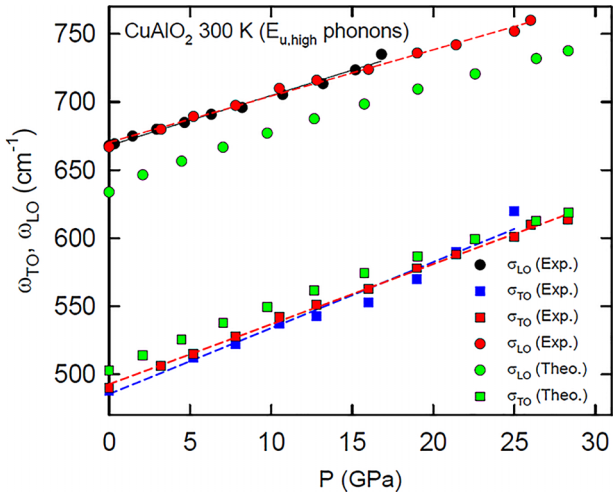

FIG. 10. Pressure dependence of the E_u^h TO-LO phonon frequencies. Experimental points for different sets of samples with their linear fits yielding pressure coefficients 4.6 ± 0.2 cm^{-1}/GPa for E_u^h (TO) and 3.4 ± 0.1 cm^{-1}/GPa for E_u^h (LO). The results of the *ab initio* calculations are also depicted, showing an overall underestimation of the E_u^h polar character, i.e., overestimate (underestimate) of TO (LO) mode frequencies. The complete linear regression results are included in Fig. 1.

Figure 10 shows the pressure dependence of the TO and LO E_u^h phonon frequencies. Both frequencies exhibit a linear behavior, with pressure coefficient 4.6 ± 0.2 cm^{-1}/GPa for E_u TO and 3.4 ± 0.1 cm^{-1}/GPa for E_u LO. Figure 10 also shows the results of the *ab initio* calculation that overestimate the frequencies of the TO mode and slightly underestimate the frequencies of the LO mode, resulting in an overall underestimation of the polar character of this phonon mode. As regards the pressure dependences, *ab initio* calculations slightly overestimate the pressure coefficient of E_u^h TO (4.8 ± 0.1 cm^{-1}/GPa) and largely overestimate the one of E_u^h LO (4.6 ± 0.1 cm^{-1}/GPa) (Fig. 1).

E. Pressure dependence of the A_{2u} high polar phonons: Transmission spectra of single crystals

Given the orientation of single crystal platelets used in this paper, optical transitions related to A_{2u} phonons are forbidden for normal incidence conditions, as incident light is polarized perpendicularly to the c axis. Nevertheless, a closer look at the transmission spectra shows that the situation is more complex. Figure 11 shows the transmission spectra of several $CuAlO_2$ single-crystal platelets at ambient pressure through the spectral range above E_u^h LO phonon frequency. These spectra exhibit a series of absorption bands, whose intensity clearly correlates to the sample thickness. It seems in principle reasonable to assign them to second-order two-phonon absorption processes. This is certainly the case of band C', as it is discussed in Sec. SM-III of the Supplemental Material [25]. Nevertheless, as we will show below, there are not IR-active two-phonon combinations at the specific frequencies of bands A' and B' that turn out to be very close to the frequencies of A_{2u}^h (TO and LO) phonons (see Fig. 1 and Table I). The fact that forbidden transitions are actually observed as weak

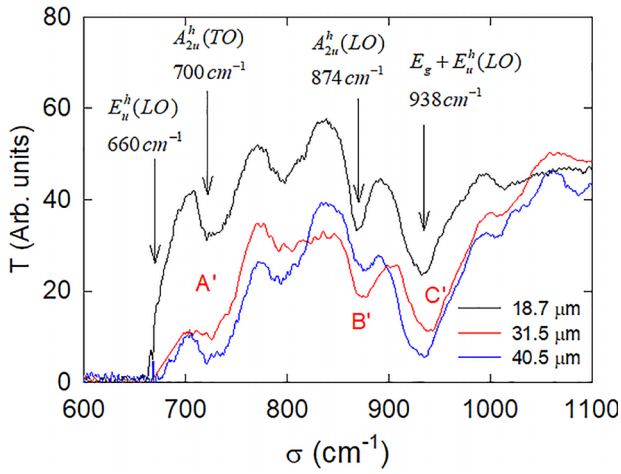

FIG. 11. Transmission spectra of several $CuAlO_2$ single-crystal platelets of different thickness through the spectral range above the E^h_u LO phonon frequency, showing a series of absorption bands A', B', and C' with intensities correlated to the sample thickness. They can be assigned to the A^h_{2u} (TO and LO) phonons and to a second-order two-phonon absorption $E_g + E^h_u$(TO).

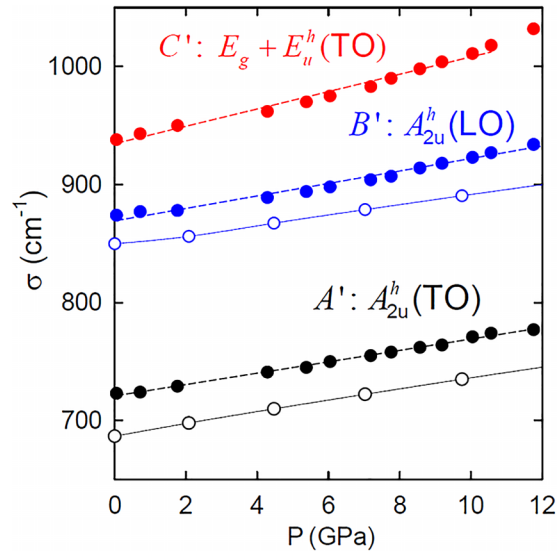

FIG. 12. Experimental frequency vs pressure (solid circles) of features A', B', and C' (in Fig. 11) and their linear fit (dashed lines) that yield coefficients 4.8 ± 0.1 cm^{-1}/GPa, 5.3 ± 0.2 cm^{-1}/GPa, and 7.3 ± 0.3 cm^{-1}/GPa respectively (Table II). The theoretically predicted pressure dependence of the A^h_{2u} (TO and LO) phonons is also shown (empty circles with solid lines).

absorption peaks can be explained by considering the geometry of Cassegrain reflective objectives. IR beams focused by this kind of objective hit the sample surface at a small angle from the surface normal. In such configuration, the beam light propagating inside the sample includes a low-intensity extraordinary beam, with a small proportion of light polarized parallel to the c axis, giving rise to a weak absorption band. This interpretation is confirmed by the behavior of these absorption bands under a sample rotation by a small angle around an axis perpendicular to the optical axis of the setup. The absorption intensity of these bands quickly increases as the rotation angle increases, consistently with the fact that rotating the sample increases the average incidence angle and then the intensity of the extraordinary ray.

Figure S3 shows the pressure evolution of the transmittance spectra of a single-crystal platelet (the 31.5-μm-thick platelet of Fig. 11) up to 12 GPa [25] The pressure dependence of the frequencies of peaks A', B', and C' is shown in Fig. 12. This figure also shows the theoretically predicted pressure dependence of A^h_{2u} (TO and LO) phonons. The pressure coefficients of peaks A', B', and C' are 4.8 ± 0.1, 5.3 ± 0.2, and 7.3 ± 0.3 cm^{-1}/GPa respectively (Table II). The pressure dependence of peaks A' and B' closely matches the predicted pressure coefficients of A^h_{2u} (TO and LO, respectively). Nevertheless, while ambient pressure B' frequency is very close to A^h_{2u} LO, the ambient pressure of both the theoretical values of A^h_{2u} TO and A' are slightly larger than the experimental value measured in Sec. III A (see Table I).

Results of the pressure dependence of the transmittance spectra of $CuAlO_2$ pellets (which, as expected, exhibit the absorption band associated with A^h_{2u} TO-LO phonon) fully confirm the assignments of peaks A' and B' in this section. Those results are presented and discussed in Sec. SM-IV of the Supplemental Material [25]. It is relevant to stress that the lack of information on both the orientation of crystallites in the powder and on the behavior of polar quasimodes [54] prevents any attempt to obtain a quantitative model of the transmission spectra.

The assignment of peak C' as an IR-active two-phonon combination is discussed in detail in Sec. SM-V [25]. Based on the direct product table of irreducible representations (IReps) of the $\bar{3}m$ point group [55], the IR-active two-phonon combinations are identified and, from its frequency at ambient pressure and pressure behavior, the C' absorption peak at 940 cm^{-1} is assigned to the $E_g + E^h_u$ double-phonon absorption.

TABLE II. Theoretical and experimental frequencies, pressure coefficients, and Grüneisen parameters of $CuAlO_2$ A^h_{2u} polar modes and two-phonon absorption peak. Wave numbers are expressed i cm^{-1}, and pressure coefficients in cm^{-1}/GPa.

	Theory			Experiment (single crystal)			Experiment (pellet)	
	σ	$\partial\sigma/\partial P$		σ	$\partial\sigma/\partial P$		σ	$\partial\sigma/\partial P$
$A^h_{2u,\mathrm{TO}}$	737 ± 7	5.0 ± 0.2	A'	721 ± 1	4.8 ± 0.1	B, C	694 ± 1	4.8 ± 0.1
$A^h_{2u,\mathrm{LO}}$	874 ± 9	5.2 ± 0.2	B'	869 ± 2	5.3 ± 0.2	F	872 ± 2	4.7 ± 0.2
$E_g + E^h_{u,\mathrm{TO}}$	920 ± 40	7.3 ± 0.3	C'	935 ± 3	7.4 ± 0.3	H	937 ± 3	7.30 ± 0.3

Finally, the behavior of the transmission spectra of the "thin" pellet for pressures larger than 32 GPa suggests that a phase transition is observed at around 32–34 GPa. This issue is discussed in detail in Sec. SM-VI [25], taking into account pressure inhomogeneity in the sample [56] and comparing with previous results on phase transitions observed in $CuAlO_2$ and related materials through other experimental techniques [23,57].

IV. CONCLUSIONS

In this paper we have investigated the pressure behavior of polar phonon modes and dielectric properties of $CuAlO_2$ delafossite by means of FTIR spectroscopy in diamond anvil-cell and *ab initio* calculations. Results at ambient pressure show that $CuAlO_2$ is a very anisotropic material in which the E_u and A_{2u} contributions to the dielectric response occur in different spectroscopic MIR intervals through which the material has hyperbolic behavior, type II (from 490 to 660 cm^{-1}) and type I (from 700 to 870 cm^{-1}). The electronic dielectric function at ambient pressure for $E \perp c$ could be determined up to the UV range (370 nm). To give quantitative account of the large dispersion in the UV range, a significant excitonic contribution had to be taken into account. Under high pressure a linear increase of the static electronic dielectric constant (for $E \perp c$) was observed. This effect is fully determined by the sample volume decrease, indicating that the electronic polarizability of $CuAlO_2$ for $E \perp c$ does not change under pressure.

The pressure behavior of the polar phonon contribution to the static dielectric constant was shown to be quite complex. In the spectral range between E_u^l and E_u^h phonons the dielectric function for $E \perp c$ exhibits an anomalously large decrease, incompatible with the Lyddane-Sachs-Teller relationship. This behavior is shown to be the result of the opposite pressure behavior of those phonon modes. While the E_u^h mode (with a large positive pressure coefficient) becomes less polar under pressure, the E_u^l mode (with a negative pressure coefficient) becomes more polar under high pressure. The static dielectric constant increases under pressure, in spite of the decrease of the E_u^h contribution, due to the increase of the electronic and E_u^l phonon contributions. For polarization parallel to the c axis, the electronic contribution is expected to be very insensitive to pressure. Given that both $A_{2u,\mathrm{TO}}^h$ (700 cm^{-1}) and $A_{2u,\mathrm{TO}}^l$ (430 cm^{-1}) phonons have positive pressure coefficients, an overall decrease of the static dielectric constant ($E \parallel c$) is expected.

In addition, a relatively intense absorption peak was observed at 935 ± 3 cm^{-1}, with a pressure coefficient of 7.4 ± 0.3 cm^{-1} GPa^{-1}. Based on its frequency and pressure coefficients the peak was assigned as an IR-active $E_g + E_u^h$ two-phonon absorption.

Finally, the pressure dependence of the absorption features associated with modes $E_{u,\mathrm{LO}}^h$ and $A_{2u,\mathrm{TO}}^h$, $A_{2u,\mathrm{LO}}^h$ up to 40 GPa, exhibit anomalies around 32 ± 2 GPa that can be reasonably attributed to the occurrence of crystal phase transition to the high-pressure phase, previously detected through Raman, XRD, and XAS experiments under high pressure.

ACKNOWLEDGMENTS

The authors acknowledge financial support from the Spanish Research Agency (AEI) and Spanish Ministry of Science and Investigation (MCIN) under Grants No. PID2019-106383GB-41/43 and No. PID2022-138076NB-C42/C44; MALTA Consolider Team Network (Grant No. RED2022-134388-T), DOI:10.13039/501100011033. This work was also supported by the Generalitat Valenciana under Grants No. PROMETEO CIPROM/2021/075-GREENMAT and No. MFA/2022/007. This study forms part of the Advanced Materials program and is supported by MCIN with funding from European Union Next Generation EU (Grant No. PRTR-C17.I1) and by the Generalitat Valenciana. The authors are grateful for assistance with the SMIS beamline at the SOLEIL synchrotron facility.

[1] H. Kawazoe, M. Yasukawa, H. Hyodo, M. Kurita, H. Yanagi, and H. Hosono, P-type electrical conduction in transparent thin films of $CuAlO_2$, Nature (London) **389**, 939 (1997).

[2] K. Ueda, T. Hase, H. Yanagi, H. Kawazoe, H. Hosono, H. Ohta, M. Orita, and M. Hirano, Epitaxial growth of transparent p -type conducting $CuGaO_2$ thin films on sapphire (001) substrates by pulsed laser deposition, J. Appl. Phys. **89**, 1790 (2001).

[3] H. Yanagi, T. Hase, S. Ibuki, K. Ueda, and H. Hosono, Bipolarity in electrical conduction of transparent oxide semiconductor $CuInO_2$ with delafossite structure, Appl. Phys. Lett. **78**, 1583 (2001).

[4] K. H. L. Zhang, K. Xi, M. G. Blamire, and R. G. Egdell, P-type transparent conducting oxides, J. Phys.: Condens. Matter **28**, 383002 (2016).

[5] X. Nie, S.-H. Wei, and S. B. Zhang, Bipolar doping and band-gap anomalies in delafossite transparent conductive oxides, Phys. Rev. Lett. **88**, 066405 (2002).

[6] J. Pellicer-Porres, A. Segura, A. S. S. Gilliland, A. Muñoz, P. Rodríguez-Hernández, D. Kim, M. S. S. Lee, and T. Y. Y. Kim, On the band gap of $CuAlO_2$ delafossite, Appl. Phys. Lett. **88**, 17 (2006).

[7] D.-S. Kim, T.-J. Park, D.-H. Kim, and S.-Y. Choi, Fabrication of a transparent p–n heterojunction thin film diode composed of p-$CuAlO_2$/n-ZnO, Phys. Status Solidi **203**, R51 (2006).

[8] A. Banerjee and K. Chattopadhyay, Electro-optical properties of all-oxide p-$CuAlO_2$/n-ZnO: Al transparent heterojunction thin film diode fabricated on glass substrate, Open Phys. **6**, 57 (2008).

[9] C.-T. Chi, I.-C. Cheng, and J.-Z. Chen, Bandgap tuning of MgZnO in flexible transparent N^+-ZnO:Al/n-MgZnO/p-$CuAlO_x$:Ca diodes on polyethylene terephthalate substrates, J. Alloys Compd. **544**, 111 (2012).

[10] B. Ling, X. W. Sun, J. L. Zhao, S. T. Tan, Z. L. Dong, Y. Yang, H. Y. Yu, and K. C. Qi, Electroluminescence from a N-ZnO Nanorod/p-$CuAlO_2$ heterojunction light-emitting diode, Phys. E (Amsterdam, Neth.) **41**, 635 (2009).

[11] B. Ling, J. L. Zhao, X. W. Sun, S. T. Tan, A. K. K. Kyaw, Y. Divayana, and Z. L. Dong, Color tunable light-emitting diodes

based on P^+-Si/p-$CuAlO_2$/n-ZnO nanorod array heterojunctions, Appl. Phys. Lett. **97**, 013101 (2010).

[12] I. Sullivan, B. Zoellner, and P. A. Maggard, Copper(I)-based p-type oxides for photoelectrochemical and photovoltaic solar energy conversion, Chem. Mater. **28**, 5999 (2016).

[13] J. Pan, Y. Sheng, J. Zhang, P. Huang, X. Zhang, and B. Feng, Photovoltaic conversion enhancement of a carbon quantum Dots/p-Type $CuAlO_2$/n-Type ZnO photoelectric device, ACS Appl. Mater. Interfaces **7**, 7878 (2015).

[14] M. Ahmadi, M. Asemi, and M. Ghanaatshoar, Mg and N co-doped $CuCrO_2$: A record breaking p-type TCO, Appl. Phys. Lett. **113**, 242101 (2018).

[15] S. Seki, Y. Onose, and Y. Tokura, Spin-driven ferroelectricity in triangular lattice antiferromagnets $ACrO_2$ (A = Cu, Ag, Li, or Na), Phys. Rev. Lett. **101**, 067204 (2008).

[16] O. Aktas, G. Quirion, T. Otani, and T. Kimura, First-order ferroelastic transition in a magnetoelectric multiferroic: $CuCrO_2$, Phys. Rev. B **88**, 224104 (2013).

[17] M. Poienar, F. Damay, C. Martin, J. Robert, and S. Petit, Spin dynamics in the geometrically frustrated multiferroic $CuCrO_2$, Phys. Rev. B **81**, 104411 (2010).

[18] M. Schmidt, Z. Wang, C. Kant, F. Mayr, S. Toth, A. T. M. N. Islam, B. Lake, V. Tsurkan, A. Loidl, and J. Deisenhofer, Exciton-magnon transitions in the frustrated chromium antiferromagnets $CuCrO_2$, α-$CaCr_2O_4$, $CdCr_2O_4$, and $ZnCr_2O_4$, Phys. Rev. B **87**, 224424 (2013).

[19] K. Park, J. Oh, J. C. Leiner, J. Jeong, K. C. Rule, M. D. Le, and J.-G. Park, Magnon-phonon coupling and two-magnon continuum in the two-dimensional triangular antiferromagnet $CuCrO_2$, Phys. Rev. B **94**, 104421 (2016).

[20] K. Kimura, H. Nakamura, S. Kimura, M. Hagiwara, and T. Kimura, Tuning ferroelectric polarization reversal by electric and magnetic fields in $CuCrO_2$, Phys. Rev. Lett. **103**, 107201 (2009).

[21] T. Aoyama, A. Miyake, T. Kagayama, K. Shimizu, and T. Kimura, Pressure effects on the magnetoelectric properties of a multiferroic triangular-lattice antiferromagnet $CuCrO_2$, Phys. Rev. B **87**, 094401 (2013).

[22] A. B. Garg and R. Rao, Copper delafossites under high pressure—a brief review of XRD and Raman spectroscopic studies, Cryst. **8**, 255 (2018).

[23] J. Pellicer-Porres, A. Segura, E. Martínez, A. M. Saitta, A. Polian, J. C. Chervin, and B. Canny, Vibrational properties of delafossite $CuGaO_2$ at ambient and high pressures, Phys. Rev. B: Condens. Matter Mater. Phys. **72**, 064301 (2005); **74**, 139902(E) (2006).

[24] J. Pellicer-Porres, D. Martínez-García, A. Segura, P. Rodríguez-Hernández, A. Muñoz, J. C. Chervin, N. Garro, and D. Kim, Pressure and temperature dependence of the lattice dynamics of $CuAlO_2$ investigated by Raman scattering experiments and *ab initio* calculations, Phys. Rev. B **74**, 184301 (2006).

[25] See Supplemental Material at http://link.aps.org/supplemental/10.1103/PhysRevB.110.104312 for the analysis of the refractive index at ambient conditions; the pressure dependence of the dielectric constants for polarization perpendicular to the c axis; the pressure dependence of the high polar phonons; the discussion of spectra obtained with the sample in pellet form; and the description of the changes observed at the phase transition.

[26] M. S. Lee, T. Y. Kim, and D. Kim, Anisotropic electrical conductivity of delafossite-type $CuAlO_2$ laminar crystal, Appl. Phys. Lett. **79**, 2028 (2001).

[27] P. Dumas, F. Polack, B. Lagarde, O. Chubar, J. L. Giorgetta, and S. Lefrançois, Synchrotron infrared microscopy at the French synchrotron facility SOLEIL, Infrared Phys. Technol. **49**, 152 (2006).

[28] R. Letoullec, J. P. Pinceaux, and P. Loubeyre, The membrane diamond anvil cell: A new device for generating continuous pressure and temperature variations, High Press. Res. **1**, 77 (1988).

[29] H. K. Mao, J. Xu, and P. M. Bell, Calibration of the ruby pressure gauge to 800 Kbar under quasi-hydrostatic conditions, J. Geophys. Res. Solid Earth **91**, 4673 (1986).

[30] J. C. Chervin, B. Canny, and M. Mancinelli, Ruby-spheres as pressure gauge for optically transparent high pressure cells, High Press. Res. **21**, 305 (2001).

[31] V. Panchal, A. Segura, and J. Pellicer-Porres, Low-cost set-up for Fourier-transform infrared spectroscopy in diamond anvil cell from 4000 to 400 cm^{-1}, High Press. Res. **31**, 445 (2011).

[32] P. Hohenberg and W. Kohn, Inhomogeneous electron gas, Phys. Rev. **136**, B864 (1964).

[33] G. Kresse and J. Furthmüller, Efficient iterative schemes for ab initio total-energy calculations using a plane-wave basis set, Phys. Rev. B **54**, 11169 (1996).

[34] P. E. Blöchl, Projector augmented-wave method, Phys. Rev. B **50**, 17953 (1994).

[35] G. Kresse and D. Joubert, From ultrasoft pseudopotentials to the projector augmented-wave method, Phys. Rev. B **59**, 1758 (1999).

[36] J. P. Perdew, A. Ruzsinszky, G. I. Csonka, O. A. Vydrov, G. E. Scuseria, L. A. Constantin, X. Zhou, and K. Burke, Restoring the density-gradient expansion for exchange in solids and surfaces, Phys. Rev. Lett. **100**, 136406 (2008).

[37] A. Togo and I. Tanaka, First principles phonon calculations in materials science, Scr. Mater. **108**, 1 (2015).

[38] R. M. Pick, M. H. Cohen, and R. M. Martin, Microscopic theory of force constants in the adiabatic approximation, Phys. Rev. B **1**, 910 (1970).

[39] S. Baroni, S. de Gironcoli, A. Dal Corso, and P. Giannozzi, Phonons and related crystal properties from density-functional perturbation theory, Rev. Mod. Phys. **73**, 515 (2001).

[40] R. P. Lowndes, Influence of lattice anharmonicity on the longitudinal optic modes of cubic ionic solids, Phys. Rev. B **1**, 2754 (1970).

[41] F. Gervais and B. Piriou, Anharmonicity in several-polar-mode crystals: Adjusting phonon self-energy of LO and TO modes in Al_2O_3 and TiO_2 to fit infrared reflectivity, J. Phys. C: Solid State Phys. **7**, 2374 (1974).

[42] M. Schubert, T. E. Tiwald, and C. M. Herzinger, Infrared dielectric anisotropy and phonon modes of sapphire, Phys. Rev. B **61**, 8187 (2000).

[43] O. S. Heavens, *Optical Properties of Thin Solid Films* (Dover Publications: New York, 1991).

[44] J. Pellicer-Porres, A. Segura, and D. Kim, Refractive index of the $CuAlO_2$ delafossite, Semicond. Sci. Technol. **24**, 015002 (2009).

[45] Note: From the condition at an interference maximum ($2nd\sigma_K = K$), a table ($2n\sigma_K$, K) can be built by using the index values at σ_K and an arbitrary sequence of correlative integers. A

linear fit of the equation $K = K_0 + d(2n\sigma_K)$ to the experimental data yields the ordinate at the origin K_0 (from which the value of the interference order can be determined) and the slope of the straight line (that is identical to the sample thickness d). The reliability of this method is larger for larger index dispersion in the explored spectral interval.

[46] J. Lekner, Reflection and refraction by uniaxial crystals, J. Phys.: Condens. Matter **3**, 6121 (1991).

[47] J. C. Phillips, Ionicity of the chemical bond in crystals, Rev. Mod. Phys. **42**, 317 (1970).

[48] J. A. Van Vechten, Quantum dielectric theory of electronegativity in covalent systems. I. Electronic dielectric constant, Phys. Rev. **182**, 891 (1969).

[49] D. R. Penn, Wave-number-dependent dielectric function of semiconductors, Phys. Rev. **128**, 2093 (1962).

[50] M. Kumar, H. Zhao, and C. Persson, Study of band-structure, optical properties and native defects in A IBIIIO$_2$ (AI = Cu or Ag, B III = Al, Ga or In) delafossites, Semicond. Sci. Technol. **28**, 065003 (2013).

[51] J. Pellicer-Porres, A. Segura, C. Ferrer-Roca, A. Polian, P. Munsch, and D. Kim, XRD and XAS structural study of $CuAlO_2$ under high pressure, J. Phys.: Condens. Matter **25**, 115406 (2013).

[52] J. Pellicer-Porres, A. Segura, and D. Santamaría-Pérez, Infrared study of $\alpha-SiO_2$ single crystal under high pressure, J. Appl. Phys. **119**, 055902 (2016).

[53] R. L. Olmon, B. Slovick, T. W. Johnson, D. Shelton, S.-H. Oh, G. D. Boreman, and M. B. Raschke, Optical dielectric function of gold, Phys. Rev. B **86**, 235147 (2012).

[54] E. Alarcón-Lladó, R. Cuscó, L. Artús, J. Jiménez, B. Wang, and M. Callahan, Raman scattering of quasimodes in ZnO, J. Phys.: Condens. Matter **20**, 445211 (2008).

[55] S. L. Altmann and P. Herzig, *Point-Group Theory Tables* (Oxford Science Publications, Oxford, 1994).

[56] S. Klotz, J. C. Chervin, P. Munsch, and G. Le Marchand, Hydrostatic limits of 11 pressure transmitting media, J. Phys. D: Appl. Phys. **42**, 075413 (2009).

[57] D. Levy, E. Greenberg, S. Layek, M. P. Pasternak, I. Kantor, S. Pascarelli, C. Marini, Z. Konopkova, and G. Kh. Rozenberg, High-pressure structural and electronic properties of $CuMO_2$ (M = Cr, Mn) delafossite-type oxides, Phys. Rev. B **101**, 245121 (2020).